Maximum Power Transfer Capability of Grid-Connected Inverters Considering Grid Strength and R/X Ratio

Guodong Liu, Michael R. Starke
Electrification and Energy Infrastructures Division,
Oak Ridge National Laboratory, Oak Ridge, TN, 37831
Email: liug@ornl.gov, starkemr@ornl.gov

***Abstract*—With the wide deployment of photovoltaic (PV) and battery energy storage systems (BESS), there has been significant number of inverters connected to the power grids, mainly the distribution grids, which are no longer ideal grids. Instead, they are considered weak grids with significant internal impedance and a less robust structure. However, the grid-connected inverters suffer from stability issues, especially under low grid strength, which limit its maximum power transfer capacity. To determine the maximum power transfer capacity of grid-connected converters, a small-signal state-space model in the synchronously rotating dq-frame of reference is established considering the grid strength, the resistance-to-reactance (R/X) ratio and detailed model of the structure and control parameters of the grid-connected inverters. Based on the established state-space model, eigenvalue analysis is performed to study the stability of grid-connected inverters. Then, the maximum power transfer capacity with small signal stability guaranteed is determined under different grid strengths and R/X ratios. Results of time-domain simulation based on switch model in Matlab/Simulink match well with that of proposed eigenvalue analysis, validating the effectiveness of the established state-space model.**

***Index Terms*—Grid-connected inverters, small-signal stability, state-space model, maximum power transfer capability**

I. Introduction

With the significant and long-term decline in photovoltaic (PV) prices (i.e., more than 50% decrease in the last decade), PV has steadily increased its dominance in the newly installed global power generation capacity. About 70% of newly installed global power generation capacity in 2024 is PV, with 38 GW record installations in the U.S. (accounting for 61% of U.S. newly installed power generation capacity) [1]. PV has generated over 30% of the electricity in the state of California and Nevada in 2024, leading the nation [2]. Meanwhile, to mitigate the fluctuations of PV and other renewable generation and ensure reliable power supply, battery energy storage system (BESS) capacity additions are accelerating, with 1 MW of storage added for every 3 MW of solar in 2024. These installed PV and BESS are connected to the grids through tens of millions of inverters, ranging from several kW residential installations to megawatt-level utility-scale installations.

The majority of grid-connected inverters for PV and BESS integration are voltage source converters (VSCs), which generate a stable AC voltage and frequency to synchronize with the grid [3]. However, VSCs are subject to stability issues, especially in weak grids, which have relatively high grid impedance and low inertia. These conditions can cause significant variations in voltage or frequency under load fluctuations or voltage flickers. Under this situation, the maximum power transfer capability of grid-connected VSCs is limited by both the VSCs' capacity and the system's stability. As the penetration of PV increases steadily, the power grid experiences reduced robustness [4]. Meanwhile, more PV projects are being deployed in locations with relatively weak grid connections, partly due to land affordability. Together, Together, these factors underscore the importance of studying the stability of grid-connected inverters.

Traditionally, small-signal stability analysis assesses a system's ability to remain stable under minor disturbances by linearizing its behavior at an equilibrium operating point. The three most widely used methods for small-signal stability analysis are: eigenvalue analysis based on a state-space model, generalized Nyquist diagrams based on an impedance model, and transfer function-based methods [5]. With full knowledge of the controller design and system configuration, a linearized state-space model can be constructed. Once built, its eigenvalues are calculated to accurately predict the system's stability boundary [6], [7]. However, this method requires comprehensive knowledge of the controller design and system configuration, which can be challenging to obtain in practical applications. In contrast, the impedance model employs measured impedance data together with the generalized Nyquist criterion (GNC) to predict the stability of the system at the AC interface [8]. Moreover, when applied to a white-box system,

This manuscript has been authored by UT-Battelle, LLC under Contract No. DE-AC05-00OR22725 with the U.S. Department of Energy.

979-8-3315-8138-1

where control design and system configuration are known, the impedance model-based method accurately predicts the stability of grid-connected inverters [9]. In [10], the multi-input-multi-output (MIMO) closed-loop transfer function of grid-connected VSCs is reduced to a single-input-single-output (SISO) open-loop transfer function, thereby enabling the use of Nyquist curves for stability analysis. In [11], virtual inductance was introduced as a means to enhance stability and improve the maximum power transfer capability of grid-connected VSCs operating in weak grids.

Most existing work investigates the stability of grid-connected VSCs under low grid strength (i.e., weak grid conditions). However, besides grid strength, the stability and maximum power transfer capability of grid-connected VSCs are also affected by the R/X ratio and the inverter's capacity limit. To address this gap, a state-space model of a grid-connected VSC is developed that considers grid strength, R/X ratios, and inverter capacity limits. Then, eigenvalue analysis is performed to investigate how these factors affect the maximum power transfer capability of grid-connected VSCs. The effectiveness of the state-space model and eigenvalue analysis is validated validated through simulations using MATLAB/Simulink. The main contributions of this paper are:

1) A state-space model of grid-connected VSCs is developed that accounts for grid strength, R/X ratios, and converter capacity limits, enabling a comprehensive stability analysis.
2) The limiting factors affecting the maximum power transfer capability of grid-connected VSCs under different grid strengths and R/X ratios are identified and validated using switch model-based simulations in MATLAB/Simulink.

Section II introduces the state-space model of the grid-connected VSCs. The maximum power transfer capability of grid-connected VSCs under various conditions are analyzed in Section III. Simulation validation is presented in Section IV. Finally, the paper is concluded in Section IV.

II. Modeling of Grid-Connected Inverter System

A. System Configuration

A simplified PV inverter connected to the AC grid is shown in Fig. 1, where R_f, L_f and C_f are the resistance, inductance and capacitance of the output filter of the inverter. R_g and L_g are the equivalent resistance and inductance of the AC grid, which are dominated by the resistance and inductance of the local distribution/transmission line. The grid strength of the system is usually quantified by a short-circuit ratio (SCR), as defined in (1), where $S_{AC} = V_{pcc}^2/Z_g$ is the short-circuit capacity of the AC grid at the point of common coupling (PCC), and S_N is the capacity of the PV inverter. The AC grid is regarded as weak when the SCR is below 3. In addition, SCR decreases (i.e., grid becomes weaker) with increasing grid impedance, e.g., longer distribution/transmission line.

$$SCR = \frac{S_{AC}}{S_N} = \frac{V_{pcc}^2}{Z_g S_N} \tag{1}$$

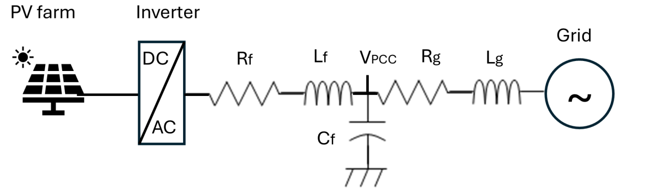

Fig. 1: Configuration of a PV inverter connected to an AC grid

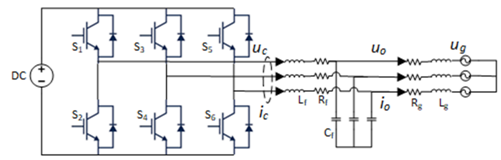

Fig. 2: Topology of grid-connected VSC

B. VSC Control Strategy

A typical topology of the grid-connected three-phase inverter is shown in Fig. 2. The ideal voltage source u_g and grid impedance R_g and L_g are connected in series, representing a weak grid. u_c and i_c are the converter output voltage and current, separately. u_o and i_o are the output voltage and current at the PCC. Generally, C_f is designed close to zero to avoid low-frequency passive resonance. Thus, $i_o \approx i_c$. The control diagram of the grid-following VSC is shown in Fig. 3, which includes an outer real power and voltage magnitude control loop, an inner d-axis and q-axis current control loop, and a phase locked-loop (PLL). The AC voltage magnitude reference is set to be the nominal value, i.e., 1 per unit. By increasing the real power reference, the maximum power transfer capability of the grid-connected VSC with stability guaranteed could be precisely determined. The controller of the grid-following VSC is designed in the rotating d-q frame, which supposes to synchronize to the voltage phase angle at the PCC (θ_o). With the phase locked-loop (PLL), the controller d-q frame is actually oriented to the PLL output θ_{pll}, which is locked with θ_o but subject to a small error. The difference between control d-q frame and the system d-q frame are illustrated in Fig. 4. For the rest of this work, the variables in the control d-q frame are indicated with the superscript '*ctrl*'.

C. VSC State-Space Model

The state-space model is built on the linearized differential equations of the system and the controller. The differential equation of the circuit between the inverter and the grid in the system d-q frame are presented as (2) - (4), which are linear.

$$\begin{cases} L_g \frac{di_{od}}{dt} = u_{od} - u_{gd} - R_g i_{od} + \omega L_g i_{oq} \\ L_g \frac{di_{oq}}{dt} = u_{oq} - u_{gq} - R_g i_{oq} - \omega L_g i_{od} \end{cases} \tag{2}$$

$$\begin{cases} C_f \frac{du_{od}}{dt} = i_{cd} - i_{od} + \omega C_f u_{oq} \\ C_f \frac{du_{oq}}{dt} = i_{cq} - i_{oq} - \omega C_f u_{od} \end{cases} \tag{3}$$

$$\begin{cases} L_f \frac{di_{cd}}{dt} = u_{cd} - u_{od} - R_f i_{cd} + \omega L_f i_{cq} \\ L_f \frac{di_{cq}}{dt} = u_{cq} - u_{oq} - R_f i_{cq} - \omega L_f i_{cd} \end{cases} \tag{4}$$

979-8-3315-8138-1

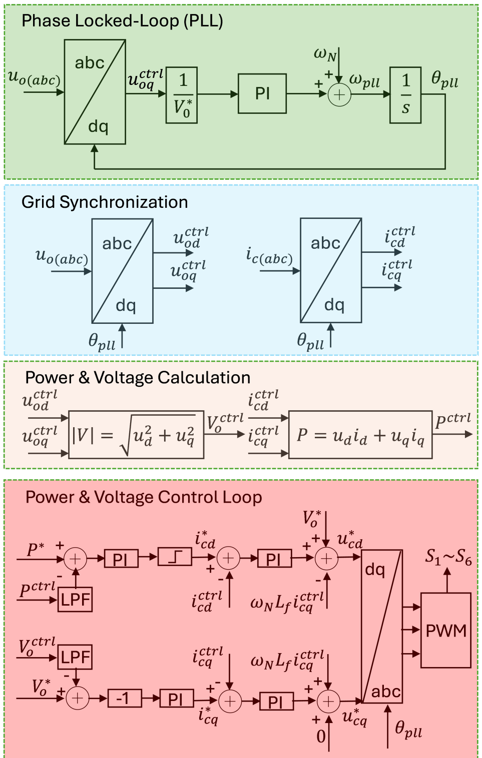

Fig. 3: Control diagram of grid-following VSC

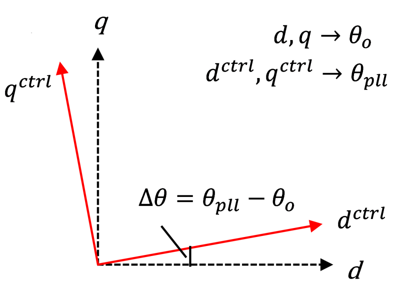

Fig. 4: Controller d-q frame and system d-q frame

Due to the small difference between the system d-q frame and the controller d-q frame, the variables of system d-q frame should be transformed to the controller d-q frame based on (5).

$$\begin{bmatrix} u_{od}^{ctrl} \\ u_{oq}^{ctrl} \end{bmatrix} = \begin{bmatrix} cos\left(\theta_{pll} - \theta_o\right) & sin\left(\theta_{pll} - \theta_o\right) \\ -sin\left(\theta_{pll} - \theta_o\right) & cos\left(\theta_{pll} - \theta_o\right) \end{bmatrix} \begin{bmatrix} u_{od} \\ u_{oq} \end{bmatrix} \tag{5}$$

The linearized small-signal equations of (5) is derived as (6) considering $\theta_{pll} \approx \theta_o$. Thus, $cos\left(\theta_{pll} - \theta_o\right) \approx 0$ and $sin\left(\theta_{pll} - \theta_o\right) \approx \theta_{pll} - \theta_o$.

$$\begin{cases} \triangle u_{od}^{ctrl} = \triangle u_{od} + u_{oq0} \triangle \theta_{pll} \\ \triangle u_{oq}^{ctrl} = \triangle u_{oq} - u_{od0} \triangle \theta_{pll} \end{cases} \tag{6}$$

Similar to (5) and (6), the variable i_{cd}^{ctrl}, i_{cq}^{ctrl}, u_{cd}^{ctrl}, and u_{cd}^{ctrl} in the controller d-q frame are derived as in (7) and (8).

$$\begin{cases} \triangle i_{cd}^{ctrl} = \triangle i_{cd} + i_{cq0} \triangle \theta_{pll} \\ \triangle i_{cq}^{ctrl} = \triangle i_{cq} - i_{cd0} \triangle \theta_{pll} \end{cases} \tag{7}$$

$$\begin{cases} \triangle u_{cd}^{ctrl} = \triangle u_{cd} + u_{cq0} \triangle \theta_{pll} \\ \triangle u_{cq}^{ctrl} = \triangle u_{cq} - u_{cd0} \triangle \theta_{pll} \end{cases} \tag{8}$$

For the inner d-axis and q-axis current control loop, differential equation (9) could be formulated.

$$\begin{cases} \frac{d \int i_d}{dt} = i_{cd}^* - i_{cd}^{ctrl} \\ \frac{d \int i_q}{dt} = i_{cq}^* - i_{cq}^{ctrl} \end{cases} \tag{9}$$

where $\int i_d$ and $\int i_q$ are state variable of the integrator in the current control loop. The output reference voltage of the current control loop is derived as in (10), , which is linear.

$$\begin{cases} u_{cd}^* = Kp\_i_d(i_{cd}^* - i_{cd}^{ctrl}) + Ki\_i_d \cdot \int i_d - \omega L_f i_{cq}^{ctrl} + V_o^* \\ u_{cq}^* = Kp\_i_q(i_{cq}^* - i_{cq}^{ctrl}) + Ki\_i_q \cdot \int i_q + \omega L_f i_{cd}^{ctrl} + 0 \end{cases} \tag{10}$$

For the outer real power and PCC voltage magnitude control loop, differential equation (11) could be formulated.

$$\begin{cases} \frac{d \int P}{dt} = P^* - P_{LPF}^{ctrl} \\ \frac{d \int V_o}{dt} = (-1)\left(V_o^* - V_{oLPF}^{ctrl}\right) \end{cases} \tag{11}$$

where $\int P$ and $\int V_o$ are state variable of the integrator in the outer real power and PCC voltage magnitude control loop, separately. P_{LPF}^{ctrl} and V_{oLPF}^{ctrl} are the real power and PCC voltage magnitude feedback after the low-pass filter (LPF). The output reference current of the outer control loop is derived as in (12), which is linear as well.

$$\begin{cases} i_{cd}^* = Kp\_P(P^* - P_{LPF}^{ctrl}) + Ki\_P \cdot \int P \\ i_{cq}^* = Kp\_V_o\,(-1)\,(V_o^* - V_{oLPF}^{ctrl}) + Ki\_V_o \cdot \int V_o \end{cases} \tag{12}$$

As shown in Fig. 3, the real power and PCC voltage magnitude are calculated as in (13).

$$\begin{cases} P^{ctrl} = u_{od}^{ctrl} i_{cd}^{ctrl} + u_{oq}^{ctrl} i_{cq}^{ctrl} \\ V_o^{ctrl} = \sqrt{\left(u_{od}^{ctrl}\right)^2 + \left(u_{oq}^{ctrl}\right)^2} \end{cases} \tag{13}$$

where (13) could be linearized as (14), considering the u_{od}^{ctrl} and u_{oq}^{ctrl} should be equal to $V_o^*$and 0, separately, in the steady state operation.

$$\begin{cases} \triangle P^{ctrl} = \triangle u_{od}^{ctrl} i_{cd0}^{ctrl} + \triangle u_{oq}^{ctrl} i_{cq0}^{ctrl} + V_o^* \triangle i_{cd}^{ctrl} \\ \triangle V_o^{ctrl} = \triangle u_{od}^{ctrl} \end{cases} \tag{14}$$

For the LPF, differential equation (15) could be formulated.

$$\begin{cases} \frac{dP_{LPF}^{ctrl}}{dt} = \omega_{LPF}\left(P^{ctrl} - P_{LPF}^{ctrl}\right) \\ \frac{dV_{oLPF}^{ctrl}}{dt} = \omega_{LPF}\left(V_o^{ctrl} - V_{oLPF}^{ctrl}\right) \end{cases} \tag{15}$$

where ω_{LPF} is the cut-off angular frequency of the LPF.

D. Phase-Locked Loop (PLL)

As shown in Fig. 3, the differential equation of PLL could be derived as in (16), which is linear.

$$\begin{cases} \frac{d \int u_{oq}}{dt} = \frac{u_{oq}^{ctrl}}{V_o^*} \\ \frac{d\theta_{pll}}{dt} = Kp\_pll \frac{u_{oq}^{ctrl}}{V_o^*} + Ki\_pll \cdot \int u_{oq} + \omega_N \end{cases} \tag{16}$$

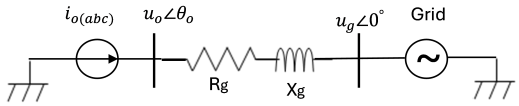

Fig. 5: Equivalent circuit of VSC connected to AC grid

TABLE I: Parameters of grid-following VSC and grid

Parameters	Values
VSC capacity	500 kVA
Grid voltage/frequency	380 V/50 Hz
Output filter capacitance	$100\mu F$
Output filter inductance/resistance	0.5 mH/0.5 mΩ
Grid resistance/inductance	0.2 mΩ/0.6 mH
Real power control loop (Kp_P, Ki_P)	(0.0114,1.1429)
Voltage magnitude control loop (Kp_V_o, Ki_V_o)	(2,100)
Inner current control loop $(Kp\_i_d/i_q, Ki\_i_d/i_q)$	(2,200)
PLL (Kp_pll, Ki_pll)	(50,1500)
ω_{LPF}	200 rad/s

E. Grid model

The equivalent circuit of the AC grid connected to the PCC of the grid-connected inverter is shown in Fig. 5.

Based on Fig. 5, the initial steady state could be calculated. According to (17), the steady state voltage phase angle at PCC θ_o could be solved. Substitute θ_o into (18), the steady state reactive power at PCC Q^* could be calculated. Then, the initial steady state u_{od0}, u_{oq0}, i_{od0}, and i_{oq0} could be calculated.

$$P^* = \frac{V_o^*}{R_g^2 + X_g^2}\left[R_g\left(V_o^* - V_g cos\theta_o\right) + X_g V_g sin\theta_o\right] \quad (17)$$

$$Q^* = \frac{V_o^*}{R_g^2 + X_g^2}\left[X_g\left(V_o^* - V_g cos\theta_o\right) - R_g V_g sin\theta_o\right] \quad (18)$$

(17) and (18) are also used to examine the capacity limit of the inverter. If the $Q^* \geq \sqrt{S^2 - P^{*2}}$, the capacity limit is violated and Q^* is limited to be $\sqrt{S^2 - P^{*2}}$, indicating voltage magnitude at the PCC might be lower than the nominal value. To boost the PCC voltage, the real power will be reduced, enforced by the current limiter of i_{cd} as in Fig. 3.

Based on the differential equations (2), (3), (4), (9), (11), (15) and (16), the state-space model of the grid-following VSC could be formulated and simply expressed as (19).

$$\triangle\dot{x}_{14\times1} = A_{14\times14}\cdot\triangle x_{14\times1} + B_{14\times2}\cdot\triangle u_{2\times1} \quad (19)$$

as $\triangle x_{14\times1} = \left[\triangle i_{od}, \triangle i_{oq}, \triangle u_{od}, \triangle u_{oq}, \triangle i_{cd}, \triangle i_{cq}, \triangle\int i_d, \triangle\int i_q, \triangle\int P, \triangle\int V_o, \triangle\int u_{oq}, \triangle\theta_{pll}, \triangle P_{LPF}^{ctrl}, \triangle V_{oLPF}^{ctrl}\right]$. The eigenvalues of the state matrix $A_{14\times14}$ indicates the small-signal stability of the grid-following VSC.

III. Eigenvalue Analysis

The state-space model of a 500 kVA grid-following VSC is built and the eigenvalue analysis is performed for stability study. The parameters of the VSC and the interconnected grid are listed in Table I. Based on this setup, the SCR is about 1.5, indicating weak grid condition and the R/X ratio is about 0.01, indicating inductive grid condition.

The eigenvalue locus as the real power at PCC varing from 5 kW to 500 kW is shown in Fig. 6, where the red circle shows the eigenvalues of the system when the PCC power reaches 500 kW. The eigenvalues move to the right-half place (i.e., the VSC becomes unstable) when the PCC power is higher than 360 kW. In other word, the maximum power transfer capacity of this grid-following VSC is about 360 kW under grid condition: $SCR = 1.5$ and $R/X = 0.01$.

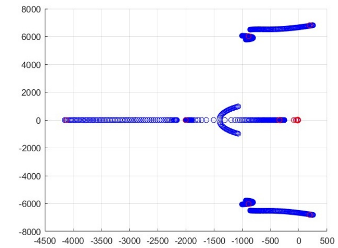

Fig. 6: Eigenvalue locus of varying PCC power (5 to 500 kW)

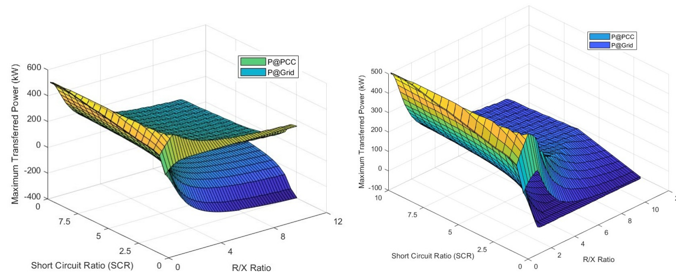

(a) P_g no limit (b) P_g non-negative

Fig. 7: Maximum power transfer capability under varying SCR and R/X ratio

The maximum power transfer capability of the grid-following VSC as well as the corresponding power received at the grid side under varying SCR and R/X ratio are shown in Fig. 7a. As can be seen, the maximum power transfer capability is high with high SCR and low R/X ratio. The maximum power transfer capability drop sharply when the SCR is below 1 (i.e., very weak grid). With the increase of R/X ratio, the maximum power transfer capability at the PCC decreases. However, the corresponding power received at the grid side changes to negative, meaning the grid side also sends power to the PCC. Both the VSC power and the grid side power are losses of the grid resistance R_g. By limiting the grid side power to be non-negative, the maximum power transfer capability is shown in Fig. 7b. These results indicate the importance of considering the R/X ration in analyzing the maximum power transfer capability of grid-following VSC.

IV. Simulation Validation

To verify the effectiveness of the eigenvalue analysis, a switch model simulation of a grid-following VSC is built in Matlab/Simulink based on parameters in Table I. The simulation results under varying SCR and R/X ratio are presented in Fig. 8. The maximum power transfer capability calculated by the switch model simulation is compared with that calculated by eigenvalue analysis as shown in Table II. The simulation results are almost same as results of eigenvalue analysis, validating the effectiveness of the eigenvalue analysis.

979-8-3315-8138-1

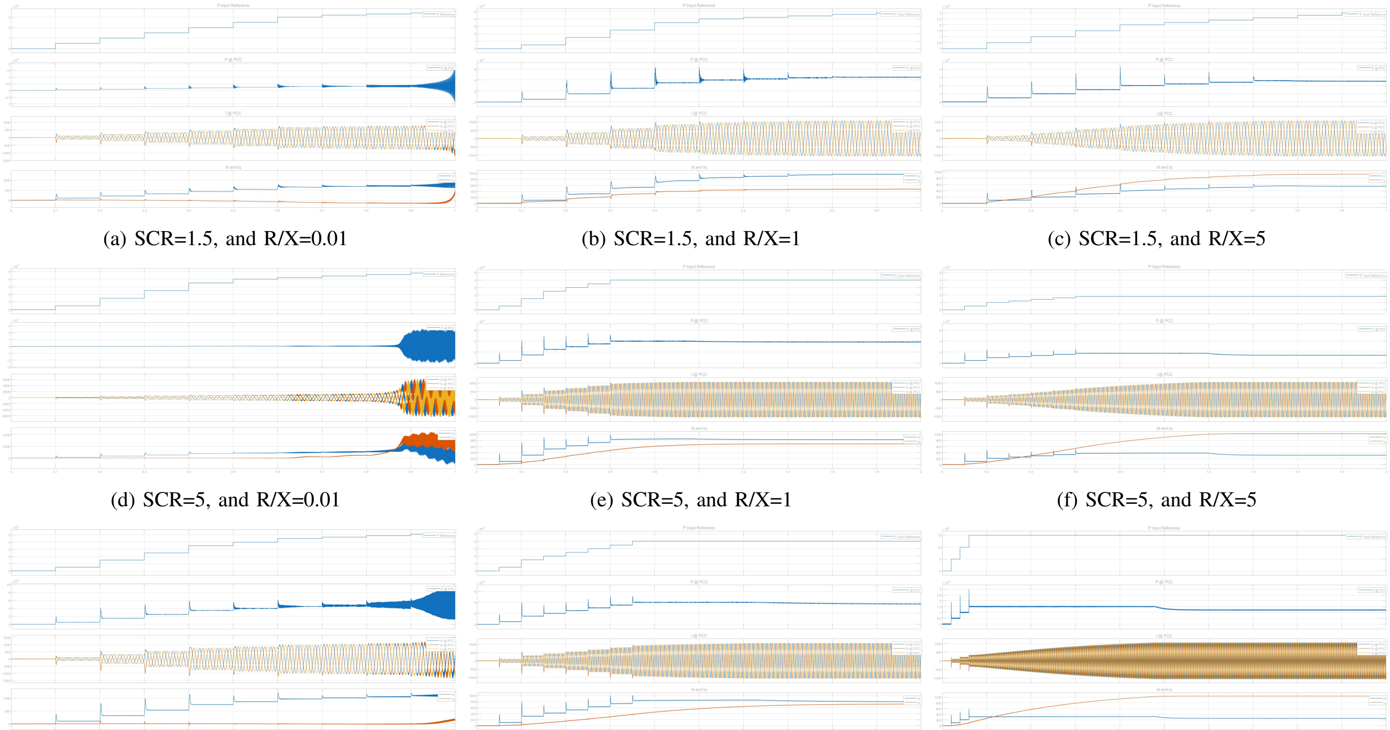

(a) SCR=1.5, and R/X=0.01 (b) SCR=1.5, and R/X=1 (c) SCR=1.5, and R/X=5

(d) SCR=5, and R/X=0.01 (e) SCR=5, and R/X=1 (f) SCR=5, and R/X=5

(g) SCR=10, and R/X=0.01 (h) SCR=10, and R/X=1 (i) SCR=10, and R/X=5

Fig. 8: Simulation results of grid-following VSC under varying SCR and R/X ratio

TABLE II: Comparison of maximum power transfer capability calculated by state-space model and switch model simulation

Maximum power transfer capability calculated by state-space model/switch model (kW)		R/X Ratio		
		0.01	1	5
SCR	1.5	360/340	450/450	255/255
	5	425/420	385/380	145/145
	10	495/480	370/370	120/120

As can be observed in Fig. 8, the power stability dominates the maximum power transfer capability of grid-following VSC when R/X ratio is small or grid resistance is neglectable (e.g., R/X=0.01). However, this dominance will be significantly weakened when the grid resistance is not neglectable (e.g., R/X$\geq$1), where the voltage stability at the PCC has dominating effects. To maintain stable nominal voltage at the PCC, the real power at PCC has to be reduced by limiting i_{cd}.

V. Conclusions

In this paper, the state-space model of a grid-connected VSC is built considering the grid strengths, R/X ratios and the capacity limit of inverters. Eigenvalue analysis is performed to investigate the effects of these factors on the maximum power transfer capability of the VSC. The effectiveness of eigenvalue analysis is validated by simulation in Matlab/Simulink. The scenario of multiple inverters (both grid-following and grid-forming) will be investigated in our future work.

References

[1] N. M. Haegel and S. R. Kurtz, "Global Progress Toward Renewable Electricity: Tracking the Role of Solar (Version 5)," IEEE Journal of Photovoltaics, vol. 15, no. 6, pp. 740-751, Nov. 2025.

[2] "Solar Market Insight Report Q2 2025", Solar Energy Industries Association (SEIA), June 2025.

[3] Y. Gui, X. Wang and F. Blaabjerg, "Vector Current Control Derived from Direct Power Control for Grid-Connected Inverters," IEEE Trans. Power Electr., vol. 34, no. 9, pp. 9224-9235, Sept. 2019

[4] F. Blaabjerg, Y. Yang, D. Yang and X. Wang, "Distributed Power-Generation Systems and Protection," Proceedings of the IEEE, vol. 105, no. 7, pp. 1311-1331, July 2017

[5] L. Huang, C. Wu, D. Zhou and F. Blaabjerg, "Comparison of Three Small-Signal Stability Analysis Methods for Grid-Following Inverter," in Proc. Int. Aegean Conf. Elect. Machines Power Electron., Int. Conf. Optim. Elect. Electron. Equip., 2021, pp. 34–41.

[6] Q. Jia, G. Yan, Y. Cai, Y. Li and J. Zhang, "Small-signal stability analysis of photovoltaic generation connected to weak AC grid," J. Modern Power Syst. Clean Energy, vol. 7, no. 2, pp. 254-267, March 2019

[7] L. Huang, C. Wu, D. Zhou, and F. Blaabjerg, "Impact of Grid Strength and Impedance Characteristics on the Maximum Power Transfer Capability of Grid-Connected Inverters," Appl. Sci., vol. 11, no. 9, 2021

[8] B. Wen, D. Boroyevich, R. Burgos, P. Mattavelli and Z. Shen, "Small-Signal Stability Analysis of Three-Phase AC Systems in the Presence of Constant Power Loads Based on Measured d-q Frame Impedances," IEEE Trans. Power Electr., vol. 30, no. 10, pp. 5952-5963, Oct. 2015

[9] L. Fan and Z. Miao, "Admittance-Based Stability Analysis: Bode Plots, Nyquist Diagrams or Eigenvalue Analysis?," IEEE Trans. Power Syst., vol. 35, no. 4, pp. 3312-3315, July 2020

[10] H. Zhang, X. Wang, L. Harnefors, H. Gong, J. -P. Hasler and H. -P. Nee, "SISO Transfer Functions for Stability Analysis of Grid-Connected Voltage-Source Converters," IEEE Trans. on Industry Appl., vol. 55, no. 3, pp. 2931-2941, May-June 2019

[11] A. Adib, F. Fateh and B. Mirafzal, "Smart Inverter Stability Enhancement in Weak Grids Using Adaptive Virtual-Inductance," IEEE Trans. Industry Appl., vol. 57, no. 1, pp. 814-823, Jan.-Feb. 2021

979-8-3315-8138-1